

Improved Anisotropic Gaussian Filters

Alex Keilmann^{1,2*}, Michael Godehardt², Ali Moghiseh², Claudia Redenbach¹ and Katja Schladitz²

^{1*}Mathematics Department, RPTU Kaiserslautern-Landau, Gottlieb-Daimler-Straße, Kaiserslautern, 67663, Germany.

²Department Image Processing, Fraunhofer ITWM, Fraunhofer-Platz 1, Kaiserslautern, 67663, Germany.

*Corresponding author(s). E-mail(s): keilmann@rptu.de;

Abstract

Elongated anisotropic Gaussian filters are used for the orientation estimation of fibers. In cases where computed tomography images are noisy, roughly resolved, and of low contrast, they are the method of choice even if being efficient only in virtual 2D slices. However, minor inaccuracies in the anisotropic Gaussian filters can carry over to the orientation estimation. Therefore, we propose a modified algorithm for 2D anisotropic Gaussian filters and show that this improves their precision. Applied to synthetic images of fiber bundles, it is more accurate and robust to noise. Finally, we demonstrate the effectiveness of our approach by applying it to real-world images of sheet molding compounds.

Keywords: Directional filter, Orientation estimation, Fiber direction, Computed tomography, Fiber reinforced polymers, Sheet molding compounds

Acknowledgements

We thank Franz Schreiber, Fraunhofer Institute for Industrial Mathematics (ITWM), for the computed tomography imaging.

1 Introduction

Gaussian filters have a wide variety of applications in image processing. Whereas isotropic Gaussian filters, being the foundation of scale space theory [1], can be implemented easily, their anisotropic counterparts are more demanding while being just as interesting [2]. They give a handle on orientation as well as scale, which makes them the cornerstones of orientation space theory [3].

Anisotropic Gaussian filters have been employed for denoising images [4, 5] as they can be adapted to image structures and, hence, preserve edges. Another application is the estimation of orientations using a filter bank of anisotropic Gaussian filters. For example, local fiber directions can be estimated by the direction of the maximal response of anisotropic Gaussian filters that are aligned along a given set of directions [6, 7]. Unlike other established methods for fiber direction estimation [8–13], this approach does not require any differentiation.

Wirjadi et al. [14] and Pinter et al. [15] both identified the Maximal Response (*MR*) method as robust to noise but suffering from the trade-off between runtime and accuracy in 3D. However, there are cases where the image quality does not allow to apply methods based on local gray-value derivatives on the one hand and where due to the production process the fibers are known to be oriented in a 2D subspace anyway. This holds for instance true for sheet molding compounds, where the reinforcing glass or carbon fibers lie within a plane. Then, only 2D images have to be analyzed. In this case, the MR method is less restricted regarding runtime and even outperforms other methods due to its robustness with respect to low image contrast [16].

The accuracy of the direction estimation clearly depends on the accuracy of the filter responses for the considered directions. Under otherwise perfect conditions, this method’s results barely depend on contrast as the filter responses scale with the contrast. Although the response differences are smaller, this does not influence which response is maximal. However, computed tomography images are often affected by noise and other artifacts. For low-contrast images, these effects have a much stronger impact on the detected direction of maximal response due to the small differences in responses for varying angles. In this case, small inaccuracies in the anisotropic Gaussian filter can impair the direction estimation further. In this paper, we will consider the case of low contrast between the foreground, i.e., fibers, and noise, while using a low resolution for the fibers.

Anisotropic Gaussian filters in \mathbb{R}^2 can be implemented naïvely by filtering in the directions of the major and the minor axis of the Gaussian’s contour ellipses, subsequently. However, Geusebroek et al. [17] derived a more accurate decomposition, where at least one of two filter directions is aligned with an axis of the image grid. Whereas the naïve implementation may need interpolation for filtering in both directions, Geusebroek et al.’s method requires interpolation for at most one filter direction. Lampert & Wirjadi [2] generalized these results to \mathbb{R}^d and provided explicit formulas for \mathbb{R}^3 .

Besides implementational inaccuracies of the 1D filters, interpolation introduces spatial inhomogeneity into the filter kernels, as Lam & Shi [18] have shown. Therefore, they propose a modification of Geusebroek et al.’s method which avoids interpolation altogether at the cost of an additional 1D Gaussian filtering step. However, Lam & Shi’s modification limits possible half-axis ratios $\omega = \frac{\sigma_2}{\sigma_1}$, to $\omega \geq 0.4142$. The ratio can be lowered to $\omega \geq 0.1622$ at the cost of aliasing effects. In our setting, far smaller ratios are needed to accurately mimic the fiber shape, e.g., $\omega = 0.025$ in Section 4.

In this paper, we therefore suggest another modification not suffering from this restriction. In Section 2, we propose modifications to Geusebroek’s decomposition that halves the number of interpolation steps. In Section 3, we show that this modification improves performance. Moreover, we consider cubic instead of linear interpolation, which improves accuracy at the cost of speed. Based on synthetic fiber images, we show that the adapted method results in higher accuracy of the maximal response method. Finally, we apply our method to a real-world image of a glass fiber sheet molding compound in Section 4 and close with a conclusion.

2 Method: Anisotropic Gaussian Filters

A natural approach to calculating the anisotropic Gaussian filter in \mathbb{R}^d is to decompose it into a sequence of multiple Gaussian filters in \mathbb{R} , which poses a simpler problem [2]. The recursive scheme with infinite impulse response by Young et al. [19–21] has proven efficient and accurate. For the case of \mathbb{R}^2 , Geusebroek et al. [17] propose a decomposition into filters along the x_1 -axis of the image grid and a filter along another direction that generally does not align with the grid.

Initially, consider an axis-aligned Gaussian kernel with standard deviations $\sigma_1 > \sigma_2 > 0$ centered in the origin, i.e.,

$$g_{\sigma_1, \sigma_2}(x_1, x_2) = \frac{1}{\sqrt{2\pi}\sigma_1} \exp\left(-\frac{1}{2} \frac{x_1^2}{\sigma_1^2}\right) \frac{1}{\sqrt{2\pi}\sigma_2} \exp\left(-\frac{1}{2} \frac{x_2^2}{\sigma_2^2}\right), \quad (1)$$

$x_1, x_2 \in \mathbb{R}.$

Its contour lines are axis-aligned ellipses with half-axis ratio $\omega = \sigma_2/\sigma_1$. We now rotate the kernel to get $g_{\sigma_1, \sigma_2, \theta}$, whose major half axis points in direction $\nu = (\cos(\theta), \sin(\theta))^T$ for $\theta \in [0, \pi)$. Formally,

$$g_{\sigma_1, \sigma_2, \theta}(x_1, x_2) = \frac{1}{\sqrt{2\pi}\sigma_1} \exp\left(-\frac{1}{2} \frac{(\mathbf{x}^T \boldsymbol{\nu})^2}{\sigma_1^2}\right) \frac{1}{\sqrt{2\pi}\sigma_2} \exp\left(-\frac{1}{2} \frac{(\mathbf{x}^T \boldsymbol{\nu}^\perp)^2}{\sigma_2^2}\right),$$

where $\mathbf{x} = (x_1, x_2) \in \mathbb{R}^2$ and $\boldsymbol{\nu}^\perp = (-\sin(\theta), \cos(\theta))^T$.

A decomposition of the corresponding filter into one-dimensional filters along the coordinate axes is generally not possible. However, Geusebroek et al. [17] proved that a decomposition into filters along the x_1 -direction and

the direction

$$\begin{aligned} \nu_* &= \nu_*(x_1, x_2, \theta, \sigma_1, \sigma_2) = x_1 \cos(\varphi) + x_2 \sin(\varphi) \quad \text{with} \\ \tan \varphi &= \frac{\sigma_2^2 \cos^2 \theta + \sigma_1^2 \sin^2 \theta}{(\sigma_1^2 - \sigma_2^2) \cos \theta \sin \theta}. \end{aligned}$$

is indeed possible, namely with the kernel

$$g_{\sigma_1, \sigma_2, \theta}(x_1, x_2) = \frac{1}{\sqrt{2\pi}\sigma_x} \exp\left(-\frac{1}{2} \frac{x_1^2}{\sigma_x^2}\right) \frac{1}{\sqrt{2\pi}\sigma_{\nu_*}} \exp\left(-\frac{1}{2} \frac{\nu_*^2}{\sigma_{\nu_*}^2}\right), \quad x_1, x_2 \in \mathbb{R}.$$

The standard deviations σ_x, σ_{ν_*} can be computed in terms of the rotation angle θ and the standard deviations σ_1, σ_2 via

$$\begin{aligned} \sigma_x &= \sigma_x(\theta, \sigma_1, \sigma_2) = \frac{\sigma_1 \sigma_2}{\sqrt{\sigma_1^2 \cos^2 \theta + \sigma_2^2 \sin^2 \theta}} \\ \sigma_{\nu_*} &= \sigma_{\nu_*}(\theta, \sigma_1, \sigma_2) = \frac{1}{\sin \varphi} \sqrt{\sigma_2^2 \cos^2 \theta + \sigma_1^2 \sin^2 \theta} \end{aligned}$$

Fig. 1 illustrates this decomposition, see [17] for the detailed derivation.

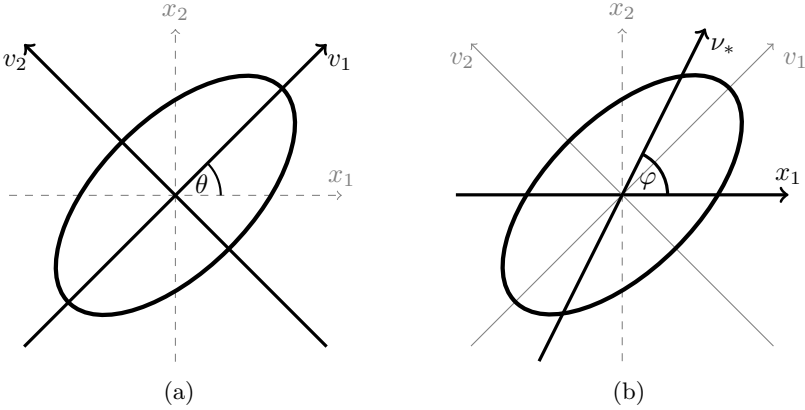


Fig. 1 The Gaussian ellipse, i.e., contour line of the Gaussian function, w.r.t. (a) the principal axes v_1 and v_2 , and (b) the axes x_1 and ν_* [17]

2.1 Algorithms for Anisotropic Gaussian Filtering

Gaussian filters can be implemented naïvely by rotating the image with the same matrix that rotates the filter such that its major and minor axes are aligned with the coordinate axes. Then, the image can be filtered along the

coordinate axes using Young et al.’s [21] recursive Gaussian filter. This way, more memory is consumed as the image does not fit its previous rectangular structure anymore. Moreover, interpolation steps are necessary for both filter directions [2].

Lampert & Wirjadi’s [2] *geometric algorithm* circumvents the interpolation along one axis by considering the filter decomposition as a shear of the coordinate axes with a shear matrix V . Hence, the image is sheared with V before filtering along the coordinate axes. Afterwards, the resulting image is transformed back with V^{-1} .

In Geusebroek et al.’s [17] *line buffer algorithm* [2] the image is processed in-place as it filters along the x_1 -axis and the ν_* -line, see above. The transformation step necessary for filtering along the ν_* -line is the inverse shear used in the geometric algorithm. This transformation using interpolation is necessary every time data is read or written. This can be kept minimal by using image line buffers for the filter history. However, as the recursive Gaussian filter consists of a forward and a backward filter, this yields 2 forward and 2 backward transformation steps, yielding 4 interpolation steps per pixel.

In comparison, the geometric algorithm uses only 2 transformations and, thus, interpolations per pixel, which makes it less error-prone compared to the line buffer algorithm. However, the geometric algorithm needs more memory because the transformed image no longer fits the original rectangular shape.

2.2 The Hybrid Algorithm

Our improved scheme combines the advantages of both the geometric and the line buffer algorithm: It filters in x_1 -direction with Young’s recursive Gaussian filter [21] as in the line buffer algorithm. The filter in ν_* -direction is modified such that the intermediate transformation steps are omitted: As the forward and backward filter move along the same line, the intermediate transformation steps taken together are the identity. Therefore, the result of the forward filter does not need to be transformed but can be stored in-place. This approach requires 2 interpolation steps per pixel, as in the geometric algorithm, while using as little memory as the line buffer algorithm. The difference to the established algorithms is ”smarter bookkeeping”. Hereafter, we will call this the *hybrid algorithm*.

An axis-aligned filter is generally more accurate than a filter that is not axis-aligned since the latter requires interpolation. Therefore, we first filter along the axis and, subsequently, in ν_* -direction.

So far, we only discussed a decomposition into filters where one filter direction is aligned with the x_1 -axis. Analogously, a decomposition such that one filter direction is aligned with the x_2 -axis is possible [2]. This may even be advantageous for $45^\circ \leq \theta \leq 135^\circ$: The standard deviation σ_x of the filter along the x_1 -axis varies over the rotation angles θ , being largest for $\theta = 0^\circ$ and smallest for $\theta = 90^\circ$. For the line buffer and the hybrid algorithm, filtering along the x_1 -axis smoothes the image in the same direction, in which the

interpolation takes place. This may be less error-prone for stronger smoothing. Hence, we propose to decompose the anisotropic filter with an x_2 -aligned axis for $45^\circ \leq \theta \leq 135^\circ$.

This modification is possible for each of the approaches mentioned above. In the following, we call this the *major-axis modification*.

2.3 Theoretical Performance Analysis

The runtime of the anisotropic Gaussian filter is constant for each pixel and depends only on the rotation angle and not on the variance. The filtering steps require 12 additions and 13 multiplications. Linear interpolation can be implemented with 1 addition and 2 multiplications per pixel.

We further propose to apply cubic interpolation with natural boundary conditions. In our implementation, each cubic interpolation step takes 8 additions and 14 multiplications per pixel. Therefore, we only combine it with the hybrid algorithm. The total complexities per pixel are listed in Table 1. The

Table 1 Complexity per pixel for different algorithms with interpolation

	Line buffer	Hybrid	
	Linear	Linear	Cubic
Multiplications	21	17	27
Additions	16	14	20

runtime of the MR method in total depends on the complexity of the employed anisotropic filter algorithm the discretization of the direction space, i.e., the number of angles considered, and the image size. The dependency on the latter three is linear, thus we discuss the speed of Gaussian filters, only.

2.4 Maximal Response of Anisotropic Gaussian Filters

To filter an image of fibers for directions, imitate the elongated shape of a fiber with the d -dimensional *anisotropic Gaussian (function)* g_θ , see Eq. 1. Its parameters give a handle on the orientation, length, and diameter for the fiber model [2].

The filter response $(g_\theta * \mathbf{f})(\mathbf{x})$ to the image \mathbf{f} is maximal when θ matches the local fiber direction in the point $\mathbf{x} \in \Xi$, where Ξ is the fiber system. Therefore, one can find the direction ν that maximizes the filter response for all $\mathbf{x} \in \Xi$ [14]:

$$\nu(\mathbf{x}) = \operatorname{argmax}_{\theta \in S^2_+} (g_\theta * \mathbf{f})(\mathbf{x})$$

$\nu(\mathbf{x})$ is estimated by calculating the convolution $(g_\theta * \mathbf{f})(\mathbf{x})$ for a finite set of directions that covers the space as evenly as possible [16]. Hereafter, we will call this the *MR method*.

3 Experimental Validation

In this section, we support the theoretical analysis with experimental results. More precisely, we show that the hybrid algorithm is more accurate than the line buffer algorithm. Employing linear interpolation, the hybrid algorithm is indeed faster than the line buffer algorithm. In the first subsection, we test the performance of anisotropic Gaussian filters as such. In the second subsection, we test performance on synthetic fiber bundles with varying noise contrast to the background.

The following experiments were carried out on an Intel(R) Core(TM) i7-7500U CPU @2.70 GHz with 16 GiB of RAM, using the GNU compiler GCC 9.0 on a 64-bit GNU/Linux operating system.

3.1 Performance of Anisotropic Gaussian Filters

In this section, we test the performance of the anisotropic Gaussian filters for the line buffer algorithm using linear interpolation, and for the hybrid algorithm using linear interpolation as well as cubic interpolation with natural boundary conditions.

3.1.1 Accuracy

We reconstruct the anisotropic Gaussian filter kernel by calculating the unit impulse response, i.e., applying the anisotropic Gaussian filter to an image of size $N \times N$ with $N = 512$, in which all pixel values are 0 except one pixel in the image center with pixel value 1. For each algorithm and variance combination considered here, we compute the l^2 -deviation between the reconstructed kernel $\hat{\mathbf{g}}_\theta$ and the actual kernel \mathbf{g}_θ as a measure of accuracy, i.e.,

$$\|\hat{\mathbf{g}}_\theta - \mathbf{g}_\theta\|_{l^2} = \left(\sum_{i,j=1}^N (\hat{g}_{\theta ij} - g_{\theta ij})^2 \right)^{\frac{1}{2}}.$$

The mean and maximum deviation for the rotation angles $\theta = 0^\circ, 1^\circ, \dots, 179^\circ$ are reported in Table 2.

The hybrid algorithm with linear interpolation yields more accurate results than the line buffer algorithm. Cubic interpolation is even more accurate, except for $\sigma_1 = 7.0, \sigma_2 = 4.0$. This is most likely due to ringing artifacts, i.e., oscillations of the interpolation kernel, which is a known problem of cubic interpolation [22] also known as the Runge phenomenon [23], or, more generally, Gibb's phenomenon [24]. However, cubic interpolation improves the approximations substantially for variance combinations that otherwise yield comparably large errors for linear interpolation. Note that smaller variances go along with larger errors because the Gaussian approximation is less precise there, see [19].

The major-axis modification achieves even higher precision compared to its counterpart without modification. Notably, the hybrid algorithm with linear

interpolation and major-axis modification often outperforms the hybrid non-modified algorithm with cubic interpolation.

Table 2 l^2 -deviation in 10^{-3} between the reconstructed and the true Gaussian kernel. Mean over all angles θ , maximal error in brackets

σ_1	σ_2	Line buffer	Hybrid		Hybrid + Mod.	
		Linear	Linear	Cubic	Linear	Cubic
2.0	1.0	38.9 (60.8)	29.7 (39.9)	23.6 (28.2)	28.0 (30.0)	25.4 (28.2)
5.0	2.0	7.2 (10.6)	6.2 (7.8)	5.8 (6.3)	5.9 (6.5)	5.7 (6.3)
7.0	2.0	5.7 (8.0)	4.9 (6.0)	4.6 (5.1)	4.6 (5.2)	4.5 (5.1)
7.0	4.0	2.8 (2.9)	2.7 (2.8)	2.6 (3.1)	2.7 (2.7)	2.6 (3.2)
10.0	0.5	35.7 (75.7)	23.1 (60.8)	14.3 (30.4)	16.9 (29.0)	12.0 (18.3)
10.0	1.25	9.5 (17.5)	7.2 (11.4)	5.9 (8.3)	5.6 (8.3)	5.4 (8.3)
10.0	2.0	4.5 (7.0)	3.9 (4.9)	3.6 (4.1)	3.6 (4.1)	3.5 (4.1)
20.0	0.5	24.6 (44.0)	15.8 (37.3)	9.8 (19.4)	10.9 (22.6)	7.7 (12.8)
20.0	1.25	6.1 (10.4)	4.6 (7.6)	3.9 (5.8)	3.4 (5.8)	3.3 (5.8)
20.0	2.0	2.9 (4.2)	2.4 (3.2)	2.3 (2.8)	2.2 (2.8)	2.1 (2.8)
25.0	0.5	21.8 (37.9)	13.9 (31.4)	8.7 (16.7)	9.6 (15.7)	6.6 (11.5)
25.0	1.25	5.5 (9.3)	4.1 (6.6)	3.4 (5.2)	2.9 (5.2)	2.8 (5.1)
25.0	2.0	2.5 (3.7)	2.1 (2.8)	2.0 (2.4)	1.8 (2.4)	1.8 (2.4)

For elongated Gaussian kernels, the l^2 -error changes considerably over all rotations: It is lowest for small angular deviations from the x -axis, that is, $\theta = 0^\circ$. Between 50° to 130° it is considerably larger, peaking around 90° . This conforms with our motivation for the major-axis modification in Section 2.2. Employing the hybrid algorithm, the deviations shrink significantly, see Fig. 2.

3.1.2 Throughput

We test the algorithms' data throughput by applying the filter 30 times to Gaussian noise images of sizes $N \times N$ with $N = 100, 130, \dots, 4990$ and calculate the trimmed mean excluding top and bottom 10%. Fig. 3 shows that the hybrid algorithm with linear interpolation is slightly faster than the line buffer algorithm, at least for larger image sizes. Cubic interpolation, however, takes considerably more time. This conforms to the theoretical results in Section 2.

The major-axis modification further slows down the algorithms. For $45^\circ \leq \theta \leq 135^\circ$, the filter in ν_* -direction iterates over all image columns, while the image pixels are saved adjacently within a line. Therefore, memory access is more expensive than it is without modification, the more so, the larger the

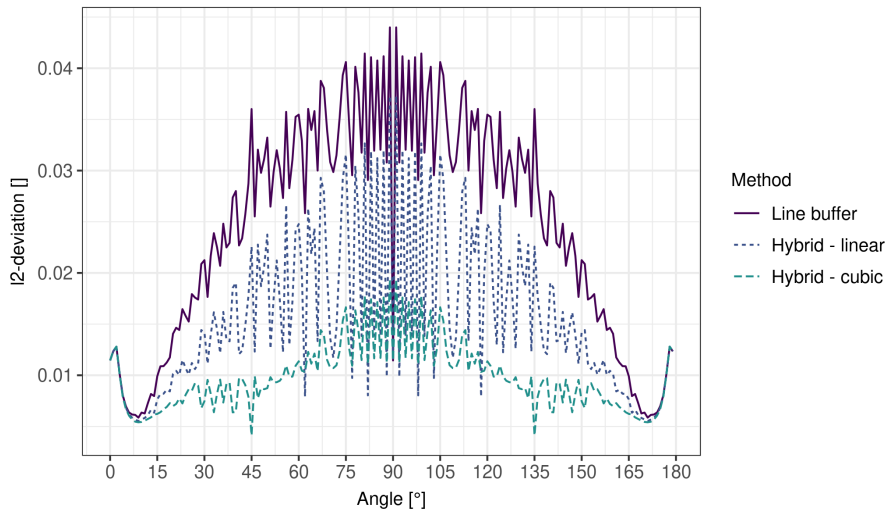


Fig. 2 l^2 -error between the reconstructed and the true Gaussian kernel with $\sigma_1 = 20, \sigma_2 = 0.5$, over all angles for the line buffer and the hybrid algorithm with linear resp. cubic interpolation

image. This can be circumvented at the cost of memory by saving the image adjacently within a column for $45^\circ \leq \theta \leq 135^\circ$.

For all three algorithms without modification, there are two different speed plateaus in the throughput, see Fig. 3. As Lampert & Wirjadi [2] argue, the throughput is dependent on the image size: In our implementations — for the hybrid as well as the line buffer algorithm — we use 4 buffers for the filter history while reading from and writing into the same image. For small image dimensions, these buffers fit into the CPU’s L1 data cache. For larger image sizes, the buffer sizes exceed the cache size slowing down the computations. In our test setup the drop at $N = 1\,690$ corresponds with the system’s size of the L1 data cache, namely 64 KiB, see Fig. 3.

3.2 Maximal Response Method

The experiments in the previous subsection have shown that anisotropic Gaussian filters are generally more accurately calculated with the hybrid than with the line buffer algorithm, especially with the major-axis modification. This section will show that these results translate to the accuracy of the MR method.

3.2.1 Setup

We evaluate the MR method on synthetic images with known constant fiber orientation. The design of the images is inspired by our application example. There, bundles of nearly parallel thin fibers form the main building block of

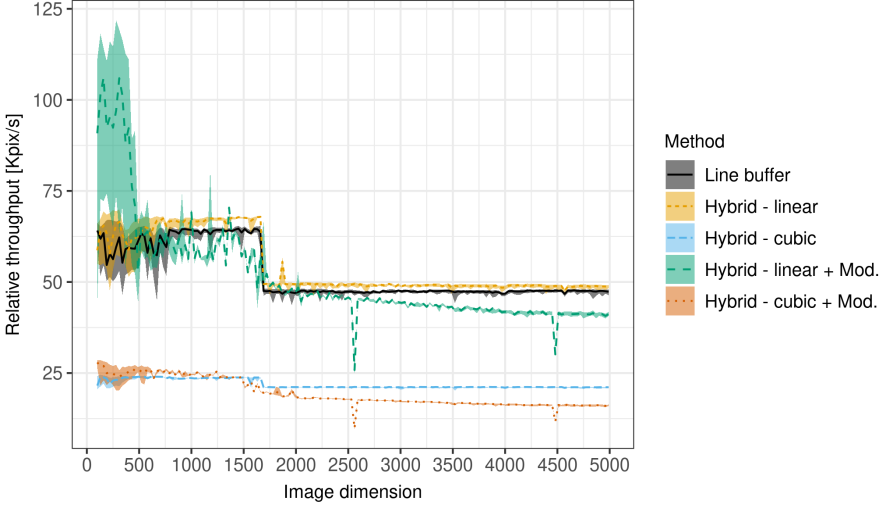


Fig. 3 Throughput of the hybrid and line buffer algorithms

the microstructure. The synthetic images shall mimic the fiber system within one such bundle.

Given an image of size 512×512 pixels, a width parameter w , and an angle θ , we define an image $F_{\theta,w}$ by setting

$$F_{\theta,w}(x,y) = \frac{\sin(x \sin(\theta) + y \cos(\theta))}{2w} + \frac{1}{2}.$$

For each $\theta = 0^\circ, 1^\circ, 2^\circ, \dots, 179^\circ$ and $w = 1, 2$, we generate such an image. These gray-value images represent idealized fiber bundles with known fiber direction and a radius of $r = \frac{\pi w}{2}$ pixels.

As background noise, we generate images B of size 512×512 with pixels sampled from the uniform distribution in $[0, 1]$.

To model images of varying contrast between background and fiber, we consider images of the form $(1 - c)B + cF_{\theta,w}$ for $c \in [0, 1]$, see Fig. 4. The MR method is applied as described below, which yields a mean absolute angular error MAE w.r.t. the known fiber direction. For comparison, we additionally apply the algorithm to images preprocessed by a median filter of size 3×3 . This is motivated by the fact that smoothing with median filters is a typical preprocessing step for real image data.

The MAE is determined as follows. The synthetic fiber image $F_{\theta,w}$ is binarized with a threshold of 0.75. The resulting image serves as a mask to include only pixels within fiber cores.

Further, we want to make sure that we only estimate the estimating bias and do not confound it with a sampling bias, i.e., lower or higher sampling probability for certain directions. For example, in an image, one can place more fibers and longer fibers in diagonal directions than in the horizontal and

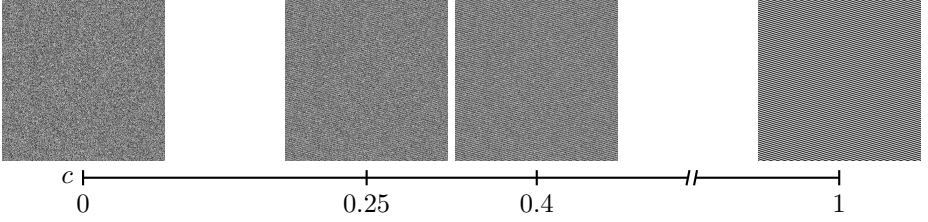


Fig. 4 Visualization of the experimental data set for varying contrast c

vertical direction. Therefore, we only evaluate pixels within a circle around the image's center. In order to avoid boundary effects, the circle radius is set to 206 pixels.

For each realization B , we are interested in the maximum of the MAE over all θ .

We run the MR method with $\sigma_1 = 20.0, \sigma_2 = 0.75w$. This is motivated by the 2σ rule for the normal distribution, which says that approximately 95% of the data points are within two standard deviations of the mean [25]. Hence, a correctly aligned filter kernel g_θ that is centered within the fiber covers the fiber's thickness with 95% of its weight when $\sigma_2 = \frac{r}{2}$, where r is the fiber's radius. Pixels that are further away than $2\sigma_2$ are barely taken into account. This ensures that the filter response is maximal when the 2-dimensional Gaussian filter kernel is aligned with the fiber: a much larger variance might take too many pixels outside of the fiber into account, while a much smaller variance results in filter kernels whose main mass is concentrated in an elliptical region that is thinner than the fibers. In this case, the ellipse might fit inside the fiber for several angles θ which makes it harder to accurately detect the point of maximum.

3.2.2 Results

Fig. 5 shows the mean error for unfiltered images as described in Section 3.2.1 and the standard deviations for 50 noise realizations. The hybrid algorithm outperforms the line buffer algorithm, especially for low-contrast cases. The cubic interpolation is more accurate than the linear interpolation, especially for the high contrast, but also for the low-contrast setup. The hybrid algorithm with linear interpolation and major-axis modification performs nearly as well as it does with cubic interpolation. For cubic interpolation, however, it performs just as well with the major-axis modification as it does without it.

Applying a median filter to noisy images is a common preprocessing step to get rid of noise while preserving edges. However, the errors are considerably larger than for unfiltered images as direction information is lost by the undirected median filter.

The effect of low contrast is reduced for the larger fiber diameter of $w = 2$ in comparison to $w = 1$.

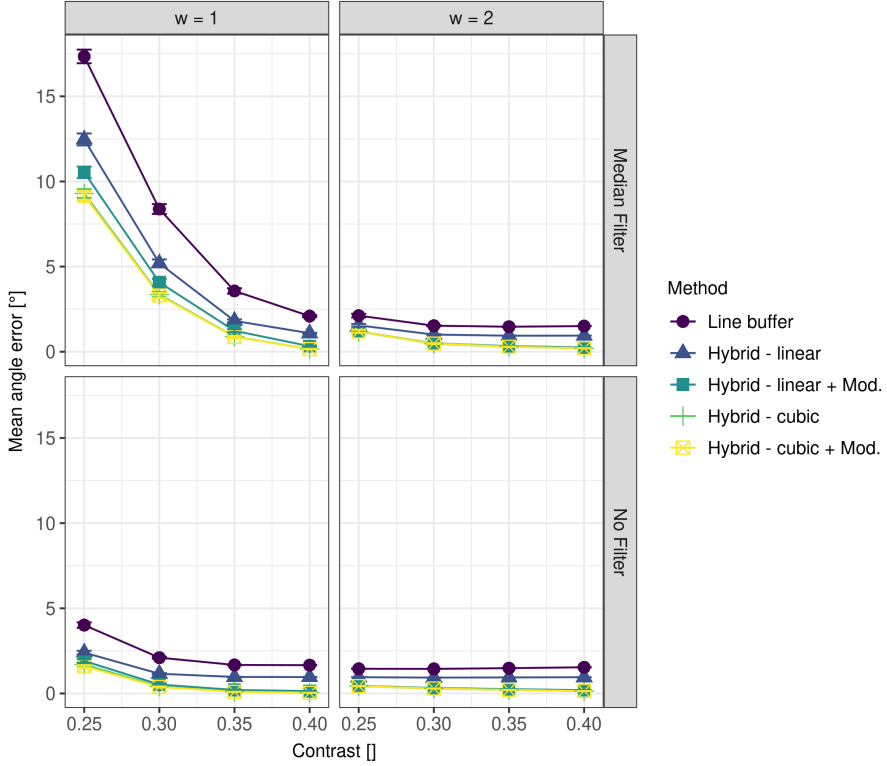


Fig. 5 Mean angle error for 50 noise images overlaid with synthetic fiber images with direction $\theta = 0^\circ, \dots, 179^\circ$, and with varying contrast. For each noise image contrast combination, the MAE's maximum over fiber directions was calculated. The mean and standard deviations over 50 noise images are depicted as point symbol with bars for each contrast and algorithm. Note, however, that the standard deviations are small and therefore the bars delimiting the interval are in most cases covered by the symbol for the mean value

4 Application

In this section, we apply the MR method to low-contrast image data of sheet molding compound materials. Sheet molding compounds (*SMC*) are a type of material consisting of stacked layers of fibers. In the automotive industry, *SMC* are of high interest due to their versatile behavior such as light weight, high stiffness, and strength, which is determined by their fiber direction distribution [26]. Computed tomography imaging of *SMC* is challenging due to the high fiber volume fraction and the low difference in X-ray absorption of fiber and matrix material.

4.1 Sheet Molding Compound with Glass Fibers

First, we consider an SMC material with glass fibers, see Fig. 6. The image was taken using the μ CT device at the Fraunhofer ITWM, Kaiserslautern, Germany, with a voltage of 120 kV, an integration time of 999 ms, and 1 200 projections/angular steps. The device uses a Feinfocus FXE-225 X-ray tube and a PerkinElmer detector with 2048×2048 pixels [27]. As specified by the manufacturer, the fibers' diameter is 10 μm . The material was scanned with a pixel spacing of 5 μm , deliberately undersampling the fibers for the sake of imaging representative sample volumes.

We applied the line buffer and the hybrid algorithm with both linear and cubic interpolation to the sample. Based on the maximal filter response, we segmented the fiber system based on Frangi et al.'s enhancement filtering [9] and a postprocessing step based on Sliseris et al.'s work [28]. Fig. 6 shows the resulting image for the hybrid algorithm with linear interpolation. The results for the other algorithm techniques are visually not distinguishable from this result. The fiber orientation tensor as defined by Advani & Tucker [29], however, indicates that the y-direction is preferred stronger when using cubic rather than linear interpolation. As the error for cubic interpolation is lower for synthetic data, we consider the result of the cubic interpolation to be the most accurate.

Table 3 Fiber orientation tensors for SMC material calculated with different algorithms

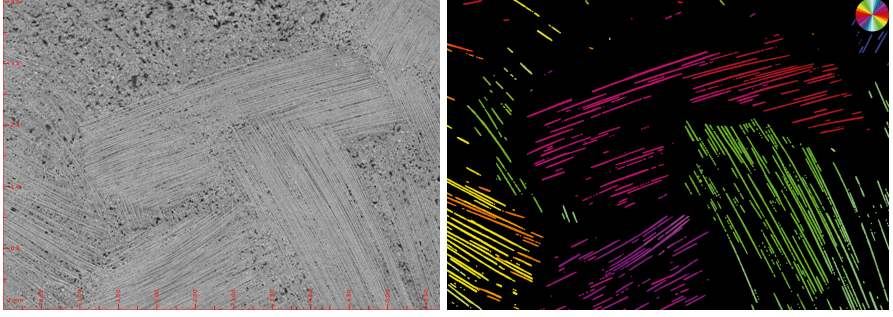
	\hat{a}_{xx}	\hat{a}_{xy}	\hat{a}_{yy}
Line Buffer	0.58	0.04	0.41
Hybrid - linear	0.58	0.04	0.41
Hybrid - cubic	0.46	0.06	0.53
Hybrid - linear + Mod.	0.49	-0.06	0.51
Hybrid - cubic + Mod.	0.49	-0.06	0.51

4.2 Sheet Molding Compound with Carbon Fibers

As a second application, we consider images of the material SMCarbon® 24 CF50-3K by POLYNT Composites Germany GmbH. It consists of carbon fibers with a length of 25 mm within a vinyl ester resin. The fiber diameter is not known directly as it also changes under pressure.

The sample was scanned with the X-ray microscope Xradia 520 by Carl Zeiss Microscopy GmbH [30] with a pixel spacing of 24.93 μm , a voltage of 60 keV, a power of 5 W, and 3 201 projections. The exposure time was 2 s, where 20 single images were taken with an exposure time of 0.1 s and then averaged. For the field-of-view, they used 76 mm \times 48 mm.

We applied the hybrid algorithm with linear interpolation and no modification and with $\sigma_1 = 25.0$, $\sigma_2 = 2.0$. Following [16], we binarized the maximal

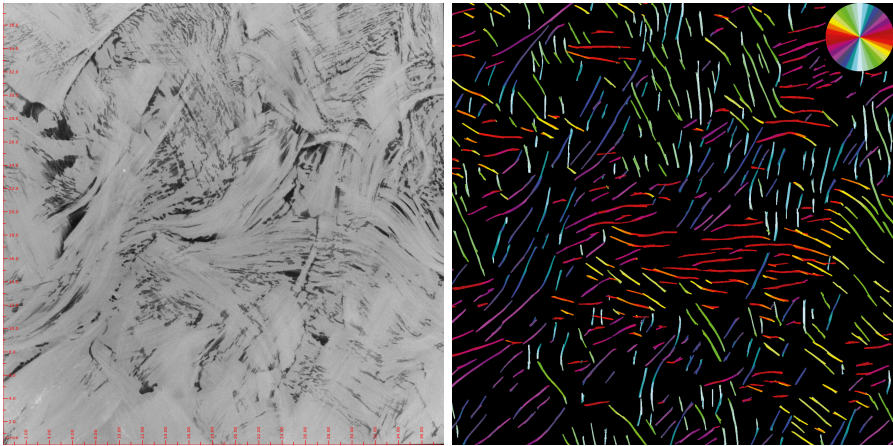


(a) Original slice, gray-values are spread for improved visibility (b) Resulting slice where the directions are color-coded, see color wheel at top-right side. The fiber mask is dilated for improved visibility

Fig. 6 Analysis of SMC with glass fibers using the MR method with $\sigma_1 = 20.0$, $\sigma_2 = 0.5$, and binarization

filter response using Niblack's local thresholding [31] with a window size of $w = 4\sigma_2$, and the threshold 0.6. Further, we excluded components that have a pixel size lower 100 after eroding the mask with a square of size 2×2 .

Despite there barely being any contrast within the fiber bundles, the MR algorithm provides a fairly accurate estimation of fiber directions.



(a) Original slice, gray-values are spread for improved visibility (b) Resulting slice, the directions are color-coded, see color wheel at top-right side

Fig. 7 Analysis of SMC with carbon fibers using the MR method with $\sigma_1 = 25.0$, $\sigma_2 = 2.0$, and binarization

5 Conclusion

We proposed an alternative algorithm for elongated anisotropic Gaussian filters in 2D, which improves throughput and accuracy. Employed in a numerical scheme for estimating fiber directions, namely the maximal response of anisotropic Gaussian filters, it improves accuracy, especially for noisy images with low contrast. We successfully applied this algorithm to real-world data sets of sheet molding compounds.

The experiments on straight and parallel fiber bundles show that our modifications yield improved precision in this case. It was inspired by the application of SMC data such as glass fibers, see Section 4.1. Note that the method still performs well on visibly bent carbon fibers, see Section 4.2.

Further improvement may be achieved with more accurate 1D Gaussian filters.

Declarations

Funding

This work was supported by the German Federal Ministry of Education and Research under Grant Agreement No: 05M22UKA.

The project in Section 4.1, named ALMA, has received funding from the European Union's Horizon 2020 Research and Innovation Programme under Grant Agreement No: 101006675.

The computed tomography scans used in Section 4.2 have been generated by the Leibniz-Institut für Verbundwerkstoffe as part of the project "C-SMC Digitalization" funded by the Fraunhofer ITWM within the framework of the High Performance Center Simulation and Software Based Innovation.

Competing Interests

The authors have no financial or non-financial interests to disclose.

Data Availability

The application data that support the findings of this study are available from the Leibniz-Institut für Verbundwerkstoffe and the ALMA project, but restrictions apply to the availability of these data, which were used under license for the current study, and so are not publicly available. Data are however available from the authors upon reasonable request and with permission of the Leibniz-Institut für Verbundwerkstoffe or the ALMA project. The experimental data generated and analyzed during this study are included in this published article and its supplementary information files.

References

- [1] Lindeberg, T.: Scale-space: A framework for handling image structures at multiple scales. CERN School of Computing **96**, 27–38 (1996)
- [2] Lampert, C.H., Wirjadi, O.: An optimal non-orthogonal separation of the anisotropic Gaussian convolution filter. IEEE Trans. Image Processing **15**(11), 3501–3513 (2006). <https://doi.org/10.1109/TIP.2006.877501>
- [3] Faas, F.G.A., van Vliet, L.J.: 3d-Orientation Space; Filters and Sampling. In: Bigün, J., Gustavsson, T. (eds.) Image Analysis, 13th Scand. Conf., SCIA 2003, Halmstad, Sweden, June 29 – July 2, 2003, Proceedings. Lecture Notes in Computer Science, vol. 2749, pp. 36–42. Springer (2003). https://doi.org/10.1007/3-540-45103-X_6
- [4] Yang, G.Z., Burger, P., Firmin, D.N., Underwood, S.R.: Structure adaptive anisotropic image filtering. Image and Vision Computing **14**(2), 135–145 (1996). [https://doi.org/10.1016/0262-8856\(95\)01047-5](https://doi.org/10.1016/0262-8856(95)01047-5)
- [5] Treece, G.: Morphology-Based Noise Reduction: Structural Variation and Thresholding in the Bitonic Filter. IEEE Trans. Image Processing **29**, 336–350 (2020). <https://doi.org/10.1109/TIP.2019.2932572>
- [6] Robb, K., Wirjadi, O., Schladitz, K.: Fiber orientation estimation from 3d image data: Practical algorithms, visualization, and interpretation. In: Proc. 7th Int. Conf. Hybrid Intelligent Systems, Kaiserslautern, Germany, pp. 320–325 (2007). <https://doi.org/10.1109/HIS.2007.26>
- [7] Wirjadi, O., Schladitz, K., Rack, A., Breuel, T.: Applications of anisotropic image filters for computing 2d and 3d-fiber orientations. In: Capasso, V., Aletti, G., Micheletti, A. (eds.) Stereology and Image Analysis - 10th European Congress of ISS, Milan, Italy, pp. 107–112 (2009)
- [8] Eberly, D., Gardner, R., Morse, B., Pizer, S., Scharlach, C.: Ridges for image analysis. J. Mathematical Imaging and Vision **4**(4), 353–373 (1994). <https://doi.org/10.1007/BF01262402>
- [9] Frangi, A.F., Niessen, W.J., Vincken, K.L., Viergever, M.A.: Multiscale vessel enhancement filtering. In: Proc. Medical Image Computing and Computer-Assisted Intervention, pp. 130–137 (1998)
- [10] Ohser, J., Schladitz, K.: 3d Images of Materials Structures – Processing and Analysis. Wiley VCH, Weinheim (2009)
- [11] Weickert, J.: Coherence-Enhancing Diffusion Filtering. Int. Journal of Computer Vision **31**, 111–127 (1999). <https://doi.org/10.1023/A:1008009714131>

- [12] Krause, M., Hausherr, J.M., Burgeth, B., Herrmann, C., Krenkel, W.: Determination of the fibre orientation in composites using the structure tensor and local x-ray transform. *J. Material Science* **45**(4), 888–896 (2010). <https://doi.org/10.1007/s10853-009-4016-4>
- [13] Altendorf, H., Jeulin, D.: 3d directional mathematical morphology for analysis of fiber orientations. *Image Analysis and Stereology* **28**(3), 143–153 (2009)
- [14] Wirjadi, O., Schladitz, K., Easwaran, P., Ohser, J.: Estimating fibre direction distributions of reinforced composites from tomographic images. *Image Analysis and Stereology* **35**(3), 167–179 (2016). <https://doi.org/10.5566/ias.1489>
- [15] Pinter, P., Dietrich, S., Bertram, B., Kehrer, L., Elsner, P., Weidenmann, K.A.: Comparison and error estimation of 3d fibre orientation analysis of computed tomography image data for fibre reinforced composites. *NDT & E Int.* **95** (2018). <https://doi.org/10.1016/j.ndteint.2018.01.001>
- [16] Schladitz, K., Büter, A., Godehardt, M., Wirjadi, O., Fleckenstein, J., Gerster, T., Hassler, U., Jaschek, K., Maisl, M., Maisl, U., Mohr, S., Netzelmann, U., Potyra, T., Steinhauser, M.: Non-destructive characterization of fiber orientation in reinforced SMC as input for simulation based design. *Composite Structures* **160**, 195–203 (2016). <https://doi.org/10.1016/j.compstruct.2016.10.019>
- [17] Geusebroek, J.-M., Smeulders, A., van de Weijer, J.: Fast Anisotropic Gauss Filtering. *IEEE Trans. Image Processing* **2350**, 938–943 (2003). https://doi.org/10.1007/3-540-47969-4_7
- [18] Lam, S.Y.M., Shi, B.E.: Recursive Anisotropic 2-d Gaussian Filtering Based on a Triple-Axis Decomposition. *IEEE Trans. Image Processing* **16**(7), 1925–1930 (2007). <https://doi.org/10.1109/TIP.2007.896673>
- [19] Young, I., Van Vliet, L.: Recursive implementation of the Gaussian filter. *Signal Processing* **44**, 139–151 (1995). [https://doi.org/10.1016/0165-1684\(95\)00020-E](https://doi.org/10.1016/0165-1684(95)00020-E)
- [20] Van Vliet, L., Young, I., Verbeek, P.: Recursive Gaussian Derivative Filters. *Proc. 14th Int. Conf. on Pattern Recognition* **1**, 509–514 (1998). <https://doi.org/10.1109/ICPR.1998.711192>
- [21] Young, I., Van Vliet, L., van Ginkel, M.: Recursive Gabor Filtering. *IEEE Trans. Signal Processing* **50**, 2798–2805 (2002). <https://doi.org/10.1109/TSP.2002.804095>
- [22] Lehmann, T.M., Gonner, C., Spitzer, K.: Survey: Interpolation Methods

- in Medical Image Processing. IEEE Trans. Medical Imaging **18**(11), 1049–1075 (1999). <https://doi.org/10.1109/42.816070>
- [23] Gautschi, W.: Numerical Analysis. Birkhäuser, Basel (2011). <https://doi.org/10.1007/978-0-8176-8259-0>
- [24] Hou, H., Andrews, H.: Cubic Splines for Image Interpolation and Digital Filtering. IEEE Trans. Acoustics, Speech, and Signal Processing **26**(6), 508–517 (1978). <https://doi.org/10.1109/TASSP.1978.1163154>
- [25] Georgii, H.-O.: Introduction to Probability and Statistics. De Gruyter, Berlin, Boston (2012). <https://doi.org/10.1515/9783110293609>
- [26] Orgéas, L., Dumont, P.J.: Sheet molding compounds. In: Wiley Encyclopedia of Composites, pp. 1–36. John Wiley & Sons Inc., Hoboken (2012). <https://onlinelibrary.wiley.com/doi/abs/10.1002/9781118097298.weoc222>
- [27] Fraunhofer ITWM: 3D-Microtomography Analysis of Microstructures. https://www.itwm.fraunhofer.de/content/dam/itwm/de/documents/BV_Infomaterial/bv_flyer_3DMikrotomografie_EN.pdf. Accessed: 2023-03-16 (2022)
- [28] Sliseris, J., Andrä, H., Kabel, M., Wirjadi, O., Dix, B., Plinke, B.: Estimation of fiber orientation and fiber bundles of MDF. Materials and Structures **49**, 4003–4012 (2015). <https://doi.org/10.1617/s11527-015-0769-1>
- [29] Advani, S., Tucker, C.: The use of tensors to describe and predict fiber orientation in short fiber composites. Journal of Rheology **31**(8), 751–784 (1987). <https://doi.org/10.1122/1.549945>
- [30] Leibniz-Institut für Verbundwerkstoffe: 3D Röntgenmikroskop. <https://www.ivw.uni-kl.de/de/forschung-entwicklung/apparative-ausstattung/3d-roentgenmikroskop>. Accessed: 2022-09-01 (2022)
- [31] Niblack, W.: An Introduction to Digital Image Processing. Prentice-Hall, Englewood Cliffs (1986)